

# Caged spin-orbit excited $I^*(^2P_{1/2}) + I^*(^2P_{1/2})$ atom pairs in liquids and in cryogenic matrices: Spectroscopy and dipolar quenching

A. V. Benderskii, R. Zadoyan, and V. A. Apkarian

Department of Chemistry, University of California, Irvine, California 92697-2025

(Received 4 April 1997; accepted 18 August 1997)

Two-photon excitation of  $I_2$  in room temperature liquid solutions and in cryogenic rare gas matrices, in the 500–600 nm range, leads to fluorescence in the near infrared. The emission spectra are assigned to the  $I^*I^*(^2P_{1/2}+^2P_{1/2}) \rightarrow I^*I(^2P_{1/2}+^2P_{3/2})$  transitions, namely, to contact pairs of spin excited atoms which are strictly bound by the solvent cage. The spectra are analyzed to characterize cage potentials and contact distances. In rare gas solids, the caged pair relaxes radiatively,  $\tau_{\text{rad}} = 3.9, 3.1,$  and  $2.8 \mu\text{s}$ , in Ar, Kr, and Xe. In room temperature liquids, emission from both geminate and nongeminate pairs occurs, resulting in bimodal kinetics. The fluorescence yield strongly depends on the nature of the solvent. Through a set of measurements in hydrogenated and deuterated solvents, the quenching mechanism is ascribed to dipolar energy transfer to solvent molecules: the quenching efficiency is determined by the spectral overlap between vibrational overtones of the solvent and the solute emission. © 1997 American Institute of Physics. [S0021-9606(97)00444-3]

## I. INTRODUCTION

Pump–probe induced fluorescence relying on the molecular ion-pair states, to probe dynamics evolving on covalent electronic surfaces, has proven a rather useful tool for time resolved studies of molecular iodine. The approach was first implemented in gas phase studies,<sup>1,2</sup> and later applied in rare gas matrices of Ar<sup>3</sup> and Kr.<sup>4</sup> Despite the fact that time resolved studies of  $I_2$  have the longest tradition in the liquid phase,<sup>5,6</sup> the same method could not be implemented there, since emission from the solvated ion-pair states is very effectively quenched in such media. Given the sensitivity of methods relying on laser induced fluorescence (LIF), and the fact that ultrafast LIF yields itself to direct interpretations as a probe of time dependent populations, fluorescence handles on this prototypical system would be valuable. The doubly spin excited states of iodine,  $I^*(^2P_{1/2}) + I^*(^2P_{1/2})$ , provide such a handle.

The interaction of two spin excited iodine atoms,  $I^*(^2P_{1/2}) + I^*(^2P_{1/2})$  leads to three strictly repulsive molecular potentials,  $0_g^+$ ,  $0_u^-$ , and  $1_u$ .<sup>7</sup> While bonding cannot be sustained on these surfaces in the gas phase, in condensed media, the pair of spin excited atoms can be stabilized at large internuclear distances per force of the solvent cage. In such a configuration, given the absence of any near lying molecular states, radiation in competition with energy transfer to solvent internal degrees of freedom serve as mechanisms of relaxation. In contrast with the atomic  $I^* \rightarrow I$  transition, which proceeds via electric quadrupole with an estimated lifetime of ~125 ms in the gas phase,<sup>8</sup> and 1–5 ms in rare gas matrices,<sup>9–11</sup> in the case of atom pairs in contact, dipole allowed transitions connect the  $I^*I^*$  states to the  $I^*I$  manifold. Accordingly, independent of the exact channel producing two  $I^*$  atoms, they will become observable upon transient encounters in the liquid phase. The situation is somewhat simpler in the solid state, where the rigid lattice traps  $I^*I^*$  pair in a state bound by the repulsive wall of the cage. We present spectra of these transitions in rare gas sol-

ids and in a variety of room temperature liquids. The spectra are analyzed to extract information about energetics and structure. The spectral analysis in the case of solids provides a direct description of the cage potentials and a critical test of many-body interactions. Time profiles and fluorescence yields are analyzed to extract information about production and decay channels of the excited states. It is established that dipolar energy transfer to vibrational overtones of the solvent serves as the main nonradiative decay mechanism of  $I^*I^*$  in the liquid phase. We follow this paper with ultrafast time resolved studies that use these transitions to probe condensed phase dynamics.

## II. EXPERIMENT

The liquid phase fluorescence spectra of iodine were obtained by two-photon excitation in the 500–600 nm range, using an excimer-pumped dye laser (Lambda Physik EMG 101/F1 2001). In some experiments, direct output of the XeCl excimer laser (308 nm) was used for fluorescence excitation. The laser outputs ~10 mJ pulses, in 10 ns, at a repetition rate of 10–20 Hz. Emission is collected at right angle, with a single quartz lens, dispersed through a 0.25 m monochromator, and detected with a liquid nitrogen cooled Ge detector (ADC Model 403H) which has a response time of 250 ns. The spectra were typically recorded at a resolution of 10–15 cm<sup>-1</sup>. Signals are processed using a digital oscilloscope (Tektronics Model 2430) or a boxcar integrator, connected to a computer. Search for emissions in the visible range (350–850 nm) was conducted using a 1 m monochromator and a photomultiplier.

The concentration of  $I_2$  in liquid solutions was monitored by measuring absorbance of the sample at 515 nm. Fluorescence efficiency in all studied solvents ( $\text{CS}_2$ ,  $\text{C}_2\text{F}_3\text{Cl}_3$ ,  $\text{CHCl}_3$ ,  $\text{CDCl}_3$ ,  $\text{CH}_2\text{Cl}_2$ ,  $\text{CD}_2\text{Cl}_2$ , acetone, acetone- $d_6$ , acetonitrile, acetonitrile- $d_6$ , hexanes, and methyltetrahydrofuran) was measured with respect to a reference  $I_2:\text{CCl}_4$  sample. Infrared absorption spectra of the neat sol-

TABLE I. Intensity of iodine ir emission in different solvents: experimental data and model of dipole–dipole quenching by solvent.

Solvent	Relative fluorescence intensity <sup>a</sup>	$\tau_{\text{rad}}$ , $\mu\text{s}$	Refractive index $n$	Spectral overlap $\int f_S(\nu) A_A(\nu) d\nu / \nu^4$ , $\text{cm}^4$	Number density, $\text{cm}^{-3}$	Fluorescence efficiency <sup>b</sup> $(1 + K_{\text{ET}} \tau_{\text{rad}})^{-1}$
Ar		$3.9 \pm 0.3$	1.27	0	$2.66 \times 10^{22}$	1
Kr		$3.1 \pm 0.2$	1.34	0	$2.22 \times 10^{22}$	1
Xe		$2.8 \pm 0.2$	1.43	0	$1.73 \times 10^{22}$	1
CS <sub>2</sub>	50	1.8 <sup>c</sup>	1.63	$< 10^{-21}$	$9.99 \times 10^{21}$	1
CF <sub>2</sub> ClFCFCl <sub>2</sub>	0.5			$< 10^{-21}$	$5.08 \times 10^{21}$	1
CCl <sub>4</sub>	1.0	2.5 <sup>c</sup>	1.46	$< 10^{-21}$	$6.22 \times 10^{21}$	1
CHCl <sub>3</sub>	0.02	2.6 <sup>c</sup>	1.448	$1.3 \times 10^{-18}$	$7.49 \times 10^{21}$	0.014
CDCl <sub>3</sub>	0.4			$5 \times 10^{-20}$		0.27
CH <sub>2</sub> Cl <sub>2</sub>	0.007	2.7 <sup>c</sup>	1.424	$2.3 \times 10^{-18}$	$9.39 \times 10^{21}$	0.006
CD <sub>2</sub> Cl <sub>2</sub>	0.24			$7 \times 10^{-20}$		0.165
Acetone	0.025	3.1 <sup>c</sup>	1.359	$2.7 \times 10^{-18}$	$8.17 \times 10^{21}$	0.005
Acetone- <i>d</i> <sub>6</sub>	0.3			$8.5 \times 10^{-20}$		0.13
CH <sub>3</sub> CN	<0.003	3.1 <sup>c</sup>	1.34	$2.3 \times 10^{-18}$	$1.10 \times 10^{22}$	0.004
CD <sub>3</sub> CN	0.04			$8 \times 10^{-20}$		0.10
Hexanes	0.01	3.0 <sup>c</sup>	1.375	$\sim 2.5 \times 10^{-18}$	$4.61 \times 10^{21}$	$\sim 0.005$
Methyl-THF	<0.005	2.8 <sup>c</sup>	1.41	$\sim 2.5 \times 10^{-18}$	$6.0 \times 10^{21}$	$\sim 0.005$

<sup>a</sup>With respect to CCl<sub>4</sub>.

<sup>b</sup>Calculated from the spectral overlap assuming the dipole–dipole quenching mechanism, Eq. (10).

<sup>c</sup>Calculated from the rare gas matrix data taking into account ratio of the refractive indices.

vents were recorded in a 1 mm thick ir quartz cell, using a commercial FT spectrometer (Bruker IFS 66).

Cryogenic rare gas matrices were prepared by vapor deposition of gas mixtures, with a typical I<sub>2</sub>:Rg mole ratio of 1:5000, onto an optical window held at 15 K by a closed-cycle helium refrigerator. The emission was collected in a collinear geometry behind the irradiated sample. The near ir region of interest in the solid state is more congested. Two-photon excitation with a femtosecond laser was useful in sorting out some of these transitions.

### III. RESULTS

#### A. Liquid phase

Infrared emission in the region 7000–9000  $\text{cm}^{-1}$  is observed upon laser excitation of room temperature solutions of I<sub>2</sub>. The set of solvents studied is listed in Table I. The emission spectra in all solvents are rather similar, consisting mainly of two structless bands, as illustrated by the examples in Fig. 1. A weak shoulder appears on the red side of the spectra in some of the solvents (CCl<sub>4</sub>, CHCl<sub>3</sub>, CH<sub>2</sub>Cl<sub>2</sub>, acetone, CH<sub>3</sub>CN). The time profile of the fluorescence is shown in Fig. 2. It consists of a detector limited rise and fall (faster than 250 ns), followed by a nonexponential tail which accounts for  $\sim 0.1$ –0.03 of the total intensity. This “slow” component decays on the time scale of 1–2  $\mu\text{s}$ , and obeys second order kinetics, with a linear dependence on I<sub>2</sub> concentration, as shown in the inset to Fig. 2. Fluorescence recorded with gated detection yields identical spectra for both “fast” and “slow” components.

Irradiation of the solutions at 308 nm (direct output of the excimer laser) was performed for CCl<sub>4</sub> and CS<sub>2</sub> and resulted in the same ir fluorescence (identical spectra and kinetics) as for the excitation in the visible. Search for emis-

sions in the visible range (350–850 nm) was performed using the same excitation, in an attempt to observe ion-pair fluorescence and double spin-flip transitions I<sup>\*</sup>I<sup>\*</sup>→II (the latter to be expected at roughly twice the frequency of the observed I<sup>\*</sup>I<sup>\*</sup>→I<sup>\*</sup>I transition). No detectable signal could be

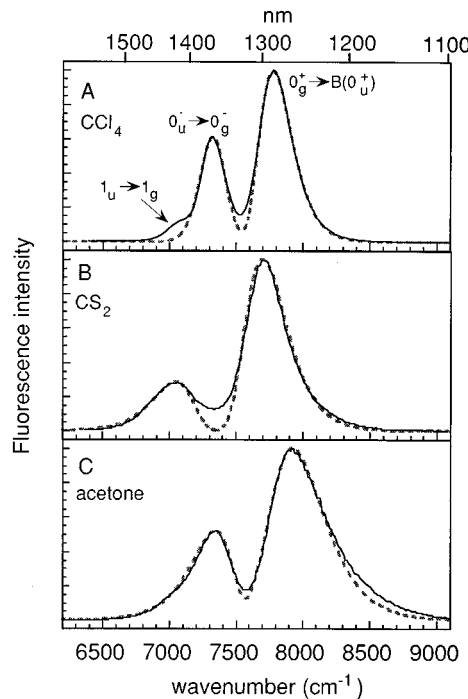


FIG. 1. Infrared fluorescence spectra of I<sub>2</sub> in room temperature solutions: (A) CCl<sub>4</sub>, (B) CS<sub>2</sub>, (C) acetone. Dashed line show spectral fits described in Sec. IV.

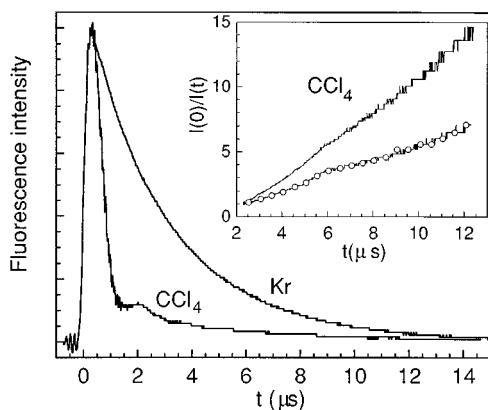


FIG. 2. Fluorescence decay kinetics in liquid solution ( $\text{CCl}_4$ ) and matrix (Kr). Inset: the “slow” component of the signal in  $\text{CCl}_4$  solution at two different concentrations showing the second-order kinetics.

found, in spite of the higher sensitivity of PMT-based detection in the visible.

The fluorescence yield varies by  $\sim 4$  orders of magnitude in the 13 solvents used, see Table I. The relative yields were calibrated in reference to a solution of  $\text{I}_2:\text{CCl}_4$ . These measurements were carried out by recording the fluorescence intensity from solutions of the same optical density. The system was calibrated with the standard (reference  $\text{CCl}_4$  sample) after each measurement to avoid errors due to variations in laser intensity and collection efficiency. The comparison makes the implicit assumption that the power dependence of this two-photon induced emission is the same in different solvents. Inspection of Table I indicates that: (a) the ir emission is very weak in hydrogen-containing solvents; (b) for a given solvent, the emission is a factor of 10–30 stronger when deuterated; (c) emission intensities in deuterated solvents are comparable to halogenated solvents (carbon tetrachloride and freon); (d) the fluorescence is exceptionally strong in  $\text{CS}_2$ .

Absorption spectra of the neat solvents, hydrogenated and deuterated counterparts, are shown in Fig. 3 for the same spectral range as the iodine fluorescence. The observed bands in the H-containing solvents can be assigned to  $2\nu(\text{C}-\text{H stretch}) + \delta(\text{bend})$ .  $\text{CS}_2$ ,  $\text{CCl}_4$ , and freon do not have any detectable absorption in the region  $5000\text{--}10000\text{ cm}^{-1}$ . The data suggests a strong correlation between fluorescence yield and spectral overlap between solute emission and solvent absorption.

## B. Matrix isolated $\text{I}_2$

Near ir fluorescence was investigated in matrix-isolated samples of  $\text{I}_2$  in Ar, Kr, and Xe at 15–30 K. Spectra recorded with a boxcar gated from 2 to  $3.5\text{ }\mu\text{s}$ , are shown in Fig. 4. The long wavelength progressions, obvious in Ar and Kr matrices, are the well known  $A \rightarrow X$  and  $A' \rightarrow X$  overlapping spectra, with the fluorescence lifetime of  $70\text{--}110\text{ }\mu\text{s}$  and  $\sim 10\text{ ms}$ , respectively.<sup>9,10,12,13</sup> In Ar, the relatively narrow emission ( $\text{FWHM} \sim 70\text{ cm}^{-1}$ ) at  $7490\text{ cm}^{-1}$ , and the broad ( $\text{FWHM} 500\text{ cm}^{-1}$ ) feature at  $8970\text{ cm}^{-1}$ , appear together.

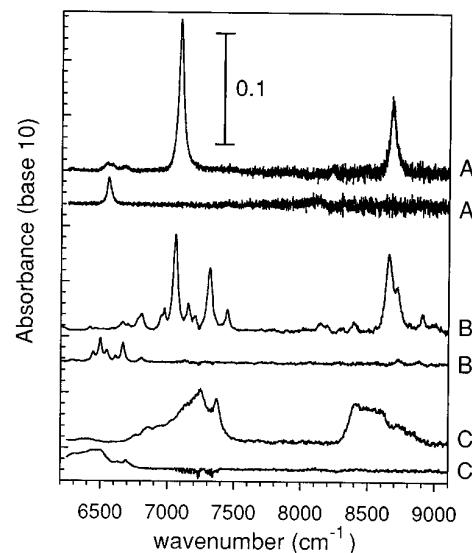


FIG. 3. Examples of infrared absorption spectra of the liquid solvents in the region of the  $\text{I}^*\text{I}^*$  emission: (A)  $\text{CHCl}_3$  and (A')  $\text{CDCl}_3$ ; (B)  $\text{CH}_2\text{Cl}_2$  and (B')  $\text{CD}_2\text{Cl}_2$ ; (C) acetone and (C') acetone- $d_6$ .

Both decay as single exponentials with a common lifetime of  $3.9 \pm 0.3\text{ }\mu\text{s}$ . Similar features are observed in Kr matrix, where the sharp and broad peaks are at  $7530$  and  $8750\text{ cm}^{-1}$ , respectively, and the intensity ratio changes in favor of the

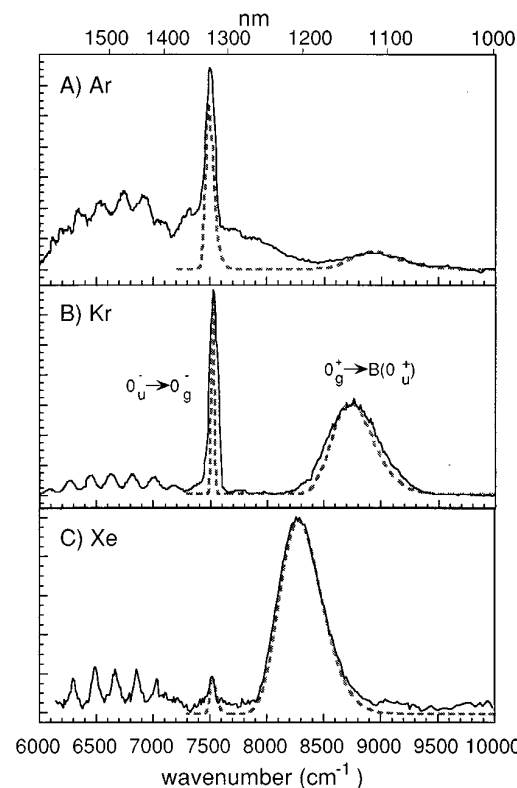


FIG. 4. Infrared fluorescence spectra of  $\text{I}_2$  in rare gas matrices: (A) Ar, (B) Kr, (C) Xe. Dashed lines show spectral simulations described in the Discussion section. Relative intensities of the simulated peaks are adjusted to fit experimental spectra.

broad feature. The fluorescence lifetime in Kr is  $3.1 \pm 0.1 \mu\text{s}$ , and the time profile is shown in Fig. 2. In Xe matrix, the two features are observed at 7510 and  $8260 \text{ cm}^{-1}$ . The intensity ratio of the two components shifts further, and the narrow peak is much weaker than the broad. In the studied spectral range of 500 to 600 nm excitation, both emissions show a two photon dependence on pump intensity. Sequential excitation using two femtosecond laser pulses showed that the fluorescence signals in the narrow and broad peaks have the same dependences on pump-probe delay, indicating that the two excited states are populated via the same excitation resonances.

#### IV. DISCUSSION

##### A. Spectroscopy

The observed ir emission spectra originate near the spin-orbit transition of atomic iodine, which occurs at 1315 nm in the gas phase.<sup>8</sup> Their assignment can be narrowed to two candidates, the single spin-flip transitions near the asymptotic region of the molecular species:  $\text{I}^*\text{I}^*\rightarrow\text{I}^*\text{I}$  or  $\text{I}^*\text{I}\rightarrow\text{I}_2$ . Indeed, other molecular states capable of producing ir fluorescence can be eliminated:  $\text{A}/\text{A}'\rightarrow\text{X}$  emission is observed in the matrices and has a much longer lifetime;<sup>9,10,12,13</sup> ion-pair states have radiative lifetimes on the order of  $10^{-8} \text{ s}$  in the gas phase<sup>14,15</sup> and may decay even faster due to non-radiative relaxation in the condensed phase. None of the observed bands can be assigned to emission of isolated atoms  $\text{I}^*\rightarrow\text{I}$ , which has been extensively analyzed previously in rare gas matrices,<sup>9</sup> and has a much longer fluorescence lifetime—from 0.25 to 1 ms, depending on temperature, in Kr and Xe matrices,<sup>11</sup> and of the order of 5 ms in Ar.<sup>9</sup> The states in the  $\text{I}^*\text{I}$  manifold can be eliminated, since the caged  $\text{I}^*\text{I}$  molecule is not expected to have a significant lifetime because it is known to recombine as  $\text{I}_2(B)$  on sub-picosecond time scales. Rather uniquely, the upper state of the observed emission must be assigned to the caged  $\text{I}^*(^2P_{1/2})\text{I}^*(^2P_{1/2})$ , and the terminal state to  $\text{I}^*(^2P_{1/2})\text{I}(^2P_{3/2})$ , as illustrated in Fig. 5. The equilibrium distance in the upper state is determined by the size of the cage, and therefore is expected to be similar to the average distance between solvent molecules (4–6 Å). Electronic states of the  $\text{I}^*\text{I}^*$  manifold are crossed by other  $\text{I}_2$  states (which correlate with  $\text{I}^*\text{I}$  and II asymptotes) at internuclear separations shorter than 3 Å.<sup>7</sup> The emitting state is therefore essentially isolated from the lower molecular states, and can relax only via radiation or energy transfer to solvent.

At the large internuclear separations implied, the optical transitions must follow strict Hund's case (c) rules, and the propensity for  $\Delta\Omega=0$  transitions must hold. A transition from each of the three upper states,  $0_g^+$ ,  $0_u^-$ ,  $1_u$ , is dipole allowed to states arising from the  $\text{I}^*\text{I}$  limit, of which there are ten. The specific transitions are: emission to the bound  $B$  state via  $\text{I}^*\text{I}^*(0_g^+)\rightarrow\text{I}^*\text{I}(B(0_u^+))$ , and emissions to the repulsive surfaces via  $\text{I}^*\text{I}^*(0_u^-)\rightarrow\text{I}^*\text{I}(0_g^-)$  and  $\text{I}^*\text{I}^*(1_u)\rightarrow\text{I}^*\text{I}(1_g)$ . Since in a given solution identical time profiles are observed for all bands, the upper states must be in fast thermal equilibrium. In the case of the cryogenic sol-

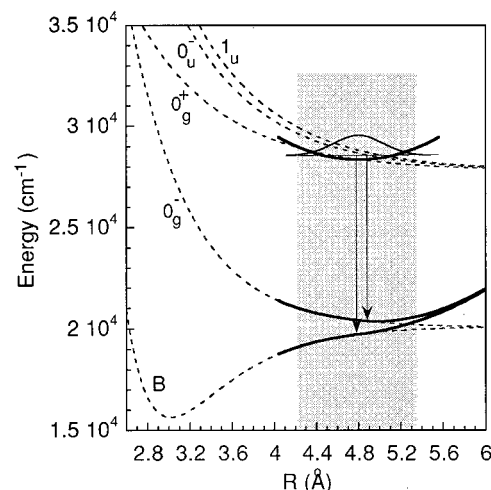


FIG. 5. Schematic diagram of potential energy curves used for spectral simulations of  $\text{I}^*\text{I}^*$  in liquid solutions (solid lines). Dashed lines show the gas phase potentials [Eqs. (2) and (4)].

ids, this would imply that the emitting states are nearly degenerate. It then follows that the blue shaded, high energy band in each spectrum must be the transition terminating on the attractive branch of the  $B$  state potential (which has negative curvature); and that the lower energy red shaded components in the liquid solutions must terminate on the repulsive  $0_g^-$  or  $1_u$  potentials. This component is rather sharp in the case of the cryogenic solids, implying nearly parallel upper and lower potentials. The observed emission peaks and their assignments are collected in Table II, where we have assumed that the ordering of  $1_u$  above  $0_g^-$  is retained in the condensed phase. Note, where observed, the  $1_u\rightarrow 1_g$  transition is a minor component in the liquids, and completely absent in the case of the solid state spectra.

Spectral simulations help to verify the consistency of the above assignments, and allow the characterization of the potentials for the cage-bound atom pairs. The bandshapes are simulated using the classical reflection approximation

$$I(\nu)=P(r;T) \frac{\delta[\nu-\Delta V(r)/h]}{d\Delta V/dr} \quad (1)$$

in which  $P(r;T)$  is the thermal probability distribution along I-I coordinate in the excited state, and  $\Delta V(r)$  is the difference potential.

In liquid solutions, only slight perturbation of the lower state potentials may be expected. We therefore use the bare  $\text{I}_2(B)$  potential in the Morse form<sup>16</sup>

$$\begin{aligned} V(B) &= D_B [1 - \exp(-\beta_B(r-r_B))]^2, \\ \text{with } D_B &= 4500 \text{ cm}^{-1}, \quad \beta_B = 1.77 \text{ Å}^{-1}, \\ \text{and } r_B &= 3.016 \text{ Å} \end{aligned} \quad (2)$$

as reference and assume a harmonic well along  $\text{I}^*\text{I}^*$  for the solvent bound upper state (Fig. 5). With the anticipation of rather shallow binding (which is confirmed since the fre-

TABLE II. Infrared fluorescence peaks and spectral fit parameters for I<sup>\*</sup>I<sup>\*</sup> in liquid solutions and rare gas matrices.

Solvent	ir fluorescence peaks, cm <sup>-1</sup>			Spectral fit parameters			
	0 <sub>g</sub> <sup>+</sup> →B	0 <sub>u</sub> <sup>-</sup> →0 <sub>g</sub> <sup>-</sup>	1 <sub>u</sub> →1 <sub>g</sub>	r <sub>nn</sub> , Å	r <sub>e</sub> , Å	ω <sub>e</sub> , cm <sup>-1</sup>	ΔT <sub>e</sub> , <sup>a</sup> cm <sup>-1</sup>
CS <sub>2</sub>	7695	7050	~6800	4.64	4.75	49	11,760
CF <sub>2</sub> Cl-CFCl <sub>2</sub>	7750	7400		5.82	4.9	53	11,855
CCl <sub>4</sub>	7775	7325	7050	5.44	4.85	50	11,855
CHCl <sub>3</sub>	7880	7310	~7050	5.11	4.75	50	11,905
CH <sub>2</sub> Cl <sub>2</sub>	7930	7270	~7040	4.74	4.70	50	11,925
Acetone	7920	7340	6950	4.97	4.65	49	11,930
CH <sub>3</sub> CN	8070	7460	~6800	4.50	4.6	53	12,005
Ar	8970	7490		3.75	4.02	75	11,970
Kr	8750	7530		4.00	4.26	58	11,900
Xe	8130	7220		4.33	4.12	62	11,150

<sup>a</sup>Energy difference between the bottom of the B state and the excited I<sup>\*</sup>I<sup>\*</sup> state minimum (the gas value 12 060 cm<sup>-1</sup>).

quency of the upper well obtained from the spectral fits is small compared to k<sub>B</sub>T—see Table II), we assume a thermal population for the upper state

$$P(r;T) = N \exp\left[-\frac{k(r-r_e)^2}{2k_B T}\right] \quad (3)$$

and a difference potential given as ΔV=ΔT'<sub>e</sub>-V''(r). ΔT'<sub>e</sub> is the difference between electronic origins of the excited state and B state. The simulated spectra of the high energy band reproduce the experiments well, see Fig. 1, fixing three parameters: the upper state equilibrium interatomic distance, r<sub>e</sub>, and harmonic force constant, k, which together define the band shape; and the electronic origin, ΔT'<sub>e</sub> (Fig. 5), which determines the transition energy. These parameters are collected in Table II, in which for convenience we report the harmonic frequency extracted from k using the reduced mass of I<sub>2</sub>.

With the upper state probability distribution, P(r;T), fixed from above, the liquid phase I<sup>\*</sup>I<sup>\*</sup>(0<sub>u</sub><sup>-</sup>)→I<sup>\*</sup>I(0<sub>g</sub><sup>-</sup>) transitions are simulated assuming an exponentially repulsive terminal state. Using the electronic origin of the upper state as a variable, the single parametrization for the terminal state

$$V(0_g^-) = 1.55 \times 10^6 \exp(-1.75r) \quad (\text{cm}^{-1}, \text{\AA} \text{ units}) \quad (4)$$

yields a satisfactory reproduction of all liquid phase spectra, as shown by the examples in Fig. 1. This provides a consistency check for the treatment, and establishes the separation between the I<sup>\*</sup>I<sup>\*</sup>0<sub>u</sub><sup>-</sup> and 0<sub>g</sub><sup>+</sup> states to be within 100–150 cm<sup>-1</sup>, in agreement with the expectation that at room temperature these states are in rapid thermal equilibrium. The intensities of the simulated bands are separately normalized to match the experiment. It is however obvious that the transition dipole moments of the two bands are nearly identical. A schematic of the liquid phase potentials is shown in Fig. 5.

The transition energies, line widths, and the separation between the main fluorescence peaks, I<sup>\*</sup>I<sup>\*</sup>(0<sub>g</sub><sup>+</sup>)→I<sup>\*</sup>I(B) and I<sup>\*</sup>I<sup>\*</sup>(0<sub>u</sub><sup>-</sup>)→I<sup>\*</sup>I(0<sub>g</sub><sup>-</sup>), are most sensitive to the contact distance, r<sub>e</sub>, between the two spin excited atoms. It is satisfying to see in Table II that indeed there is a direct correlation

between r<sub>e</sub> and the average intermolecular distance between solvent molecules (r<sub>nn</sub>=1.12ρ<sup>-1/3</sup>, where ρ is the number density of the neat solvent). In the densest liquids, CS<sub>2</sub> and CH<sub>3</sub>CN, r<sub>e</sub> is somewhat larger than r<sub>nn</sub>. Although smaller than r<sub>nn</sub>, the largest values of r<sub>e</sub>=4.85 Å occur in the least dense liquids, CCl<sub>4</sub> and CF<sub>2</sub>Cl-CFCl<sub>2</sub>. This correlation is a most direct confirmation of the picture of the upper state as a solvent bound contact pair. The upper state harmonic frequencies provide an additional confirmation. The liquid phase frequencies, about 50 cm<sup>-1</sup>, fall well within the translational spectra. In short, the I<sup>\*</sup>-I<sup>\*</sup> interactions are no stronger than the intermolecular attractive forces between solvent molecules, and therefore the observed upper state is a diffusion controlled contact pair.

In rigid cryogenic matrices, contrary to liquids, perturbations of the I<sub>2</sub> molecular potentials by the cage of surrounding rare gas atoms are expected to be significant. We therefore start with the potentials calculated by Batista and Coker<sup>17</sup> using diatomics-in-molecules (DIM) Hamiltonian for I<sub>2</sub> in the doubly substituted site of undistorted fcc rare gas lattice, which are presented in Fig. 6. Since in the cryogenic matrices hν>k<sub>B</sub>T, we use the scaled temperature

$$T' = \frac{\hbar\omega}{2k_B} \left[ \tanh\left(\frac{\hbar\omega}{2k_B T}\right) \right]^{-1} \quad (5)$$

for the calculation of P(r;T). Note, due to the cryogenic temperature, transitions sample a much smaller range of internuclear distances (shaded region in Fig. 6) than in room temperature liquids (shaded region in Fig. 5).

The main qualitative features of the spectrum: the broad, high energy I<sup>\*</sup>I<sup>\*</sup>(0<sub>g</sub><sup>+</sup>)→I<sup>\*</sup>I(B) band and narrow lower frequency I<sup>\*</sup>I<sup>\*</sup>(0<sub>u</sub><sup>-</sup>)→I<sup>\*</sup>I(0<sub>g</sub><sup>-</sup>) transition, are reproduced well for all matrices using unmodified Batista-Coker potentials. The solid state I<sup>\*</sup>I<sup>\*</sup>(0<sub>u</sub><sup>-</sup>)→I<sup>\*</sup>I(0<sub>g</sub><sup>-</sup>) emissions are much narrower than in the liquids, reflecting the fact that the cage induced potentials for both upper and lower states are nearly aligned vertically, and have similar curvatures, as is evident from Fig. 6.

For Ar matrix, the DIM potentials provide a good quantitative reproduction of the experimental spectrum, only re-

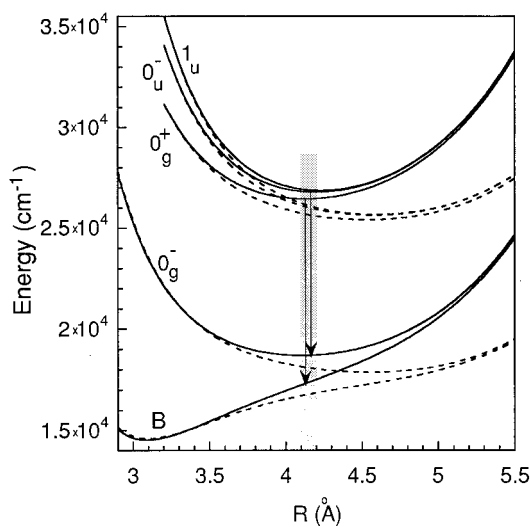


FIG. 6. Cage potentials for  $I_2$  in Xe matrix used for spectral simulations. Dashed lines: unmodified DIM potentials for  $I_2$  molecule in doubly substituted site of perfect fcc Xe lattice by Batista and Coker (Ref. 17). Solid lines: potentials (6) and (7) (parameters in Table III) which produce spectral fit shown in Fig. 4.

quiring a vertical shift of the electronic origin by  $500\text{ cm}^{-1}$  to the red for both bands. The calculated spectrum is shown in Fig. 4(A). For Kr and Xe matrices, however, Batista–Coker potentials do not provide quantitative reproduction of experimental spectra, giving a  $0_g^+ \rightarrow B$  band that is too narrow (especially in the case of Xe,  $220\text{ cm}^{-1}$  calculated FWHM vs  $450\text{ cm}^{-1}$  experimental). The predicted separation between the two main peaks are only  $630$  and  $450\text{ cm}^{-1}$ , respectively, as compared with the experimental values  $1200$  and  $750\text{ cm}^{-1}$  for Kr and Xe. This suggests that the actual internuclear separations in the excited state are smaller than those predicted by the DIM calculation ( $4.31\text{ \AA}$  in Kr double site and  $4.5\text{ \AA}$  in Xe), i.e., requires smaller cage.

To simulate the spectra, we approximated the DIM potentials separating them into contributions from the I–I and I–RG interactions, which allows to model a smaller cage by horizontally shifting the I–RG part of the potential. The parametrization of potentials is presented in Table III. The  $B$  state potential is represented in the form

$$V = D_B [1 - \exp(-\beta_B(r - r_B))]^2 + D_c [1 - \exp(-\beta_c(r_c - r))]^2, \quad (6)$$

where I–I interaction is given by a Morse function with parameters only slightly modified with respect to those used for simulation in liquids [Eq. (2)], and I–RG part of the potential is modeled by a reflected Morse function. Repulsive I–I states [upper states  $I^*I^*(0_g^+ \text{ and } 0_u^-)$  and terminal state  $I^*I(0_g^-)$ ] were represented by

$$V = A \exp(-\gamma r) + D_c [1 - \exp(-\beta_c(r_c - r))]^2 \quad (7)$$

with a single exponential function for repulsive  $I^*$ –I or  $I^*$ – $I^*$  interaction. For each matrix, all parameters were first optimized to fit the Batista–Coker potentials. As can be seen in Table III, slightly different sets of parameters in the I–RG part of the potential (Table III) were used for the states of  $I^*I$  and  $I^*I^*$  manifolds, reflecting different interactions of the I and  $I^*$  with the host. For the one-dimensional cage potentials in the form (6)–(7), change of the parameter  $r_c$  by the same amount for the upper and lower states (i.e., horizontally shifting the I–RG part) is equivalent to changing the size of the cage.<sup>18</sup> This results in a shift of the upper potential minimum  $r_e$  and change of the simulated spectral band shape, because of the change in the difference potential. Experimental spectra were therefore fitted by adjusting the parameter  $r_c$ , which determines the position of the cage wall, simultaneously for the upper and lower state. Spectral fits obtained in this way are shown in Fig. 4, and the upper state parameters, determined from thus obtained potentials (6) and (7), are collected in Table II. For Kr, only a slight change of  $r_e$

TABLE III. Parametrization of the caged potentials for  $I_2$  in rare gas matrices. For  $B$  state  $V = D_B [1 - \exp(-\beta_B(r - r_B))]^2 + D_c [1 - \exp(-\beta_c(r_c - r))]^2$ ; for repulsive states  $V = A \exp(-\gamma r) + D_c [1 - \exp(-\beta_c(r_c - r))]^2$ .

Manifold	Potential	Parameter	Ar	Kr	Xe
$I^*I$	Cage	$D_c, \text{ cm}^{-1}$	1000	2600	4700
		$\beta_c, \text{ \AA}^{-1}$	0.755	0.56	0.46
		$r_c, \text{ \AA}$	3.33 (3.33) <sup>a</sup>	3.95 (4.10) <sup>a</sup>	3.95 (4.50) <sup>a</sup>
	$B$	$D_B, \text{ cm}^{-1}$	4500	4500	4500
		$\beta_B, \text{ \AA}^{-1}$	1.67	1.67	1.67
		$r_B, \text{ \AA}$	3.05	3.05	3.05
$I^*I^*$	$0_g^-$	$A, \text{ cm}^{-1}$	$1 \times 10^7$	$1 \times 10^7$	$1 \times 10^7$
		$\gamma, \text{ \AA}^{-1}$	2.40	2.47	2.47
		$D_c, \text{ cm}^{-1}$	1100	2800	4800
	$0_g^+$	$\beta_c, \text{ \AA}^{-1}$	0.76	0.585	0.49
		$r_c, \text{ \AA}$	3.33 (3.33) <sup>a</sup>	3.9 (4.05) <sup>a</sup>	3.87 (4.42) <sup>a</sup>
		$A, \text{ cm}^{-1}$	$2.2 \times 10^6$	$2.2 \times 10^6$	$2.2 \times 10^6$
$0_u^-$	$0_u^-$	$\gamma, \text{ \AA}^{-1}$	1.96	1.96	1.96
		$A, \text{ cm}^{-1}$	$6 \times 10^6$	$6 \times 10^6$	$6 \times 10^6$
	$1_u$	$\gamma, \text{ \AA}^{-1}$	2.12	2.12	2.13

<sup>a</sup>Values obtained by fitting the experimental spectra. In parenthesis—value for the unmodified Batista–Coker potential.

(from 4.31 to 4.26 Å) is required to obtain good agreement. In Xe,  $r_e$  must be changed from 4.5 to 4.12 Å in order to reproduce the width of the  $0_g^+ \rightarrow B$  band. The I\*I\* caged potentials in Xe, which give spectral fits presented in Fig. 4(C), are compared in Fig. 6 with the unmodified DIM potentials of Batista and Coker. We note, however, that the potentials listed in Table III are to be trusted only around the region of the internuclear I–I separations sampled by the studied transitions,  $r_e \pm 0.1$  Å (see Table II for  $r_e$  values). Furthermore, separation of the caged potentials into the I–I and I–RG contributions was devised only as a way to obtain equilibrium I\*–I\* distance in the upper state implied by the spectra; the I–I and I–RG parts therefore do not have any physical meaning if used separately.

## B. Photogeneration

Prior to discussing the decay mechanisms, the photogeneration pathways deserve some comment. There are a variety of resonant two-photon entrance channels to the I\*I\* potentials when using visible  $ns$  lasers. Coherent excitation with  $B(^3\Pi_{0u})$  and  $B''(^1\Pi_1)$  states acting as real intermediates can lead to the dense manifold of dissociative states that correlate either directly with the I\*+I\* limit, or with the I\*I limit. The latter states invariably cross the I\*–I\* potentials. Alternatively, the sequential two photon path,  $X \rightarrow B \rightarrow E$  exists, which involves vertical excitation to the repulsive wall of the  $B$  state, a short time evolution on  $B$  to reach the right turning point of the potential, and subsequent resonant excitation to the  $E(0_g)$  ion-pair state. Finally, excitation to  $B$ , predissociation via one of the many curve crossings, and subsequent excitation to either the I\*I\* potentials or the manifold of ion-pair states is possible. As already mentioned, the ion-pair states of I<sub>2</sub> do not fluoresce in the liquid phase, and solvent induced predissociation into the I\*I\* manifold constitutes one of the major channels of quenching. This occurs because of the differential solvation of ionic versus neutral states in dielectric media. A crude estimate of the electronic solvation energy,  $E_s$ , of the ion-pair states can be made via the Onsager cavity model<sup>19</sup>

$$E_s = \frac{8\mu^2}{d^3} \left( \frac{\epsilon - 1}{2\epsilon + 1} \right) \approx \frac{e^2}{r_e} \left( \frac{\epsilon - 1}{2\epsilon + 1} \right) \quad (8)$$

in which  $\epsilon = n^2$  is the dielectric constant of the solvent;  $\mu \approx er_e$ , is the dipole of the ion-pair state with a bondlength  $r_e \sim 3.6$  Å; and we have assumed the cavity diameter,  $d$ , to be given as  $2r_e$ . On this basis, it can be estimated that in the most polarizable solvent, in CS<sub>2</sub>, the ion-pair states will be lowered by ~1 eV, generating crossings with the I\*I\*( $1_u, 0_u$ ) potentials. In the next most polarizable solvent, in CCl<sub>4</sub>, the estimated electronic solvation,  $E_s \sim 0.85$  eV, brings the ion-pair states close enough to the I\*I\* potentials, to expect solvent mediated coupling between them. In the less polarizable solvents, a direct curve crossing between ionic and neutral manifolds is not expected. These considerations seem to explain, in part, the observation that the ir

emissions in CS<sub>2</sub> is a factor of 50 stronger than in CCl<sub>4</sub>, and that emission in the latter is stronger than all others (see Table I).

## C. Kinetics of the upper state

The remarkably different decay kinetics of the I\*I\* infrared fluorescence in solid matrices and liquid solutions (Fig. 2) can now be understood. In matrices, the potential barrier for the cage escape of I\* atoms is many eV, ensuring the complete caging of photogenerated atoms. Crossings with the repulsive states of the I\*+I and I+I manifolds occur in the region 2.5–3.5 Å (see Fig. 1), far from the emitting minimum near 4–4.5 Å. Accordingly, there are no nonradiative decay channels for the decay of the excited state population. The observed exponential decay in matrices must be ascribed to radiation. The fluorescence lifetimes in Ar, Kr, and Xe matrices ( $3.9 \pm 0.3$  μs,  $3.1 \pm 0.2$  μs, and  $2.8 \pm 0.3$  μs, respectively), corrected for the refractive index of the medium<sup>20</sup> (Table II), all yield the same value of  $7.0 \pm 0.5$  μs for the hypothetical gas phase radiative lifetime, representing dipole coupling of the I\*I\* and I\*I surfaces at ~4.5 Å separation.

In contrast, in the room temperature liquids, given the fact that I\*–I\* interactions are no stronger than I\*–solvent interactions, it can be surmised that I\* atoms will escape the cage via a diffusional barrier, comparable to that experienced by solvent molecules during self-diffusion. Assuming a typical liquid phase diffusion coefficient of  $10^{-5}$  cm<sup>2</sup>/s, a barrier height of  $E_b = 1500$  cm<sup>-1</sup> can be estimated, implying a lifetime on the order of  $10^{-9}$  s for an I\*–I\* contact pair. The cage escape probability upon photogeneration is determined by the initial excess kinetic energy,  $E_{\text{kin}} = 2000–5000$  cm<sup>-1</sup>, which is larger than the estimated barrier height. Accordingly, a distribution of spatially separated I\*–I\* pairs,  $\rho(R,0)$ , in fast kinetic equilibrium with the I\*I\* contact pairs,  $\rho(R_0,0)$ , is to be expected. The thermalization length for an I\* atom can be obtained from the number of collisions with the solvent molecules necessary to damp its initial kinetic energy. In a solution such as CCl<sub>4</sub>, because of the similarity in masses, the collisional energy exchange is highly efficient (~50% per collision), and thermalization within  $n = (\ln 2)^{-1} \ln [E_{\text{kin}} - E_b]/k_B T \sim 3–5$  collisions may be expected. Assuming random walk thermalization ( $l \sim R_0 + a_0 n^{1/2}$ ), the characteristic length of the initial distribution can be determined as  $1 \sim 10–15$  Å. The diffusion of I\* atoms in solution governs time evolution of their pair distribution function  $\rho(R,t)$  which, in turn, determines the population of the emitting state  $\rho(R_0,t)$ . Because the average initial separation in I\*–I\* pairs is smaller than the distance between the precursor I<sub>2</sub> molecules in solution (on the order of 1 μm), there are two distinct contributions to the kinetics. Encounters between geminate pairs dominate at short times, and homogeneous second-order encounter kinetics of spatially randomized I\* atoms determines the long-time behavior. This explains the experimentally observed fluorescence decay profiles in liquids. The decay time scale for the geminate encounter can be estimated from the diffusion equation

as  $\alpha l^2/D$ , with the coefficient  $\alpha \sim 0.35$  for the 3-dimensional case. This gives  $\tau_{\text{gem}} \sim 0.5-1$  ns, so that the observed “fast” component of the signal is given by the response function of the detector. The “slow” component of the signal can be well fit with second order kinetics  $C(0)/C(t) = 1 + k_D t$ , as illustrated in the inset in Fig. 3. The diffusion-limited rate constant  $k_D = 4\pi DR_0 C(0)$  can be rationalized for  $C(0) \sim 10^{17} \text{ cm}^{-3}$ , which implies that only about 1% of the iodine concentration in the sample contributes to the “slow” component. Extrapolation of the “slow” component to  $t=0$  accounts for less than 1/5 of the “fast” signal.

#### D. Dipolar quenching

Figure 2 and Table I demonstrate that the  $I^*I^*$  fluorescence is quenched when ir absorption bands of the solvent overlap the emission spectrum. The role of spectral overlap in determining fluorescence yields is best isolated by the comparisons in the isotopically substituted solvent pairs. In the solvent pairs considered,  $\text{CHCl}_3/\text{CDCl}_3$ ,  $\text{CH}_2\text{Cl}_2/\text{CD}_2\text{Cl}_2$ , acetone/acetone- $d_6$ ,  $\text{CH}_3\text{CN}/\text{CD}_3\text{CN}$ , the fluorescence yield in the hydrogenated solvent is more than an order of magnitude weaker than in the deuterated version. The spectra in Fig. 3 illustrate that deuteration shifts the solvent absorption bands out of overlap with the solute emission. Quenching due to resonant energy transfer from the spin-orbit excited iodine to vibrational overtones of the solvent molecules is the obvious explanation. The rate of such a process is given by the Förster expression for dipole-dipole energy transfer between a donor and an acceptor<sup>21</sup>

$$K_{\text{ET}} = \frac{1.685 \times 10^{-4} \kappa^2}{l N n^4} \frac{1}{R^6} \frac{1}{\tau_{\text{rad}}} \int A_A(\nu) f_E(\nu) \frac{d\nu}{\nu^4}. \quad (9)$$

Here  $\tau_{\text{rad}}$  is the radiative lifetime of the donor,  $f_E(\nu)$  its emission spectrum normalized to unity,  $A_A(\nu)$  the decadic absorbance of the acceptor molecules of number density  $N(\text{cm}^{-3})$  measured through pathlength  $l$  ( $l=0.1$  cm for spectra shown in Fig. 3),  $\nu$  frequency in  $\text{cm}^{-1}$ ,  $R$  the distance between the donor and acceptor,  $n$  refractive index of the medium. The orientation factor  $\kappa^2$  is equal to 2/3 for random directional distribution of the transition dipoles. The fluorescence efficiency is  $(1 + K_{\text{ET}}\tau_{\text{rad}})^{-1}$ . In our case, any of the solvent molecules can serve as an acceptor, and the total quenching rate is obtained by summation over all surrounding solvent molecules, hence

$$K_{\text{ET}}\tau_{\text{rad}} = \sum_i K_{\text{ET}}(R_i)\tau_{\text{rad}} \\ = \frac{1.123 \times 10^{-4}}{\ln^4} I \int 4\pi R^{-4} g(R) dR, \quad (10)$$

where  $g(R)$  is the radial distribution function of solvent molecules around  $I^*I^*$  emitter and  $I$  denotes the spectral overlap integral in Eq. (9).

The spectral overlap integrals in Eq. (9) for different solvents were calculated numerically from the experimental absorption and emission spectra and are presented in Table I. For H-containing solvents, emission spectra recorded in their

deuterated counterparts were used because of the better signal-to-noise ratio (the spectra in H/D pairs of solvents are identical). For non-H-containing solvents ( $\text{CCl}_4$ ,  $\text{CS}_2$ , and freon) the listed values are only upper estimates because no detectable solvent absorption was recorded in the spectral range of the emission. The  $1/R^6$  integral of Eq. (10) was estimated using analytical approximation of the radial distribution function for Lennard-Jones spheres, with  $\sigma$  parameter scaling according to the number density of the corresponding solvent:  $\sigma \propto N^{-1/3}$ . The calculated values of the fluorescence efficiency  $(1 + K_{\text{ET}}\tau_{\text{rad}})^{-1}$  are listed in Table I. Good agreement with the experimental fluorescence intensities is achieved for the series of similar solvents  $\text{CCl}_4$ ,  $\text{CHCl}_3$ ,  $\text{CDCl}_3$ ,  $\text{CH}_2\text{Cl}_2$ ,  $\text{CD}_2\text{Cl}_2$ . There is also good correlation in pairs acetone/acetone- $d_6$  and  $\text{CH}_3\text{CN}/\text{CD}_3\text{CN}$ . We can be confident that the dipole-dipole excitation transfer is responsible for the quenching of fluorescence.

The relative fluorescence intensity is higher for acetone by a factor of 2.6 (slower ET) and lower for acetonitrile by a factor of 2.5 (faster ET) than the values for  $\text{CH}_n\text{Cl}_{4-n}$  group. It is, of course, hard to compare different solvents because the excitation efficiency may vary depending on the position of the solvated ion-pair states, as discussed above. There are, however, several factors neglected in our crude model that also can explain the aforementioned discrepancies and are worth discussing. Because of the sharp  $1/R^6$  dependence of the transfer rate, it is very sensitive to the local structure of the solvent around the sensitizer. Molecules of the first coordination shell (first peak of the radial distribution function) contribute more than 95% to the integral in Eq. (10); therefore even a small error in estimating the position and height of the first peak of  $g(R)$  would change the ET rate significantly. Orientation of the solvent molecules surrounding the  $I_2$  emitter can also affect the excitation transfer. First, the factor  $\kappa^2$  in Eq. (9) may be different from 2/3 if dipoles are not randomly oriented. Second, the excitation transfer distance  $R$  really is the distance between transition dipoles, which, in case of  $2\nu(\text{C}-\text{H stretch}) + \delta(\text{bend})$  overtone vibration of solvent molecules, is likely to be centered on the C-H bond. Thus orientation of the C-H groups of the solvent molecules towards or away from the  $I_2$  solute may alter  $R$  by as much as  $\pm 1.5 \text{ \AA}$ , which may result in the change in the ET rate by a factor of  $[(5+1.5)/(5-1.5)]^6 \approx 40$ . For example, the observed fluorescence intensities in acetone and acetonitrile can be brought into agreement with those for  $\text{CH}_n\text{Cl}_{4-n}$  group (even assuming equal excitation efficiency) if one accepts the excitation transfer distance of 4  $\text{\AA}$  in acetonitrile and 7.5  $\text{\AA}$  in acetone, compared with the values of 4.5 and 5  $\text{\AA}$  from the number densities of these solvents.

The dipole-dipole mechanism is usually invoked for excitation transfer between chromophore molecules with strong transitions. In this case, large transition dipole moments make possible the excitation transfer over distances as long as  $R_0 \sim 50-100 \text{ \AA}$  (Förster radius). Thus energy transfer rates can be used for measuring distances between chromophores for geometrical characterization of biological molecules,<sup>22</sup> polymers,<sup>23</sup> films<sup>24</sup> and membranes,<sup>25</sup> etc. In our system, on the contrary, both donor and acceptor transi-

tions are very weak (radiative lifetimes  $\sim 3 \mu\text{s}$  and  $\sim 1 \text{s}$ ; respectively, compared to a typical value of 1 ns for a strong chromophore). However, efficient excitation transfer is possible because of the short distances between acceptor and sensitizer (about 6 orders of magnitude gain in  $1/R^6$  compared to a typical value of the Förster radius) and the number of acceptors ( $\sim 10$  in the first coordination shell). About 2 orders of magnitude are gained in the spectral overlap integral [Eq. (9)] because of the lower transition frequency (ir vs vis), which brings the ET rate to about  $10^6 \text{ s}^{-1}$ , compared to  $10^9 \text{ s}^{-1}$  for the typical case of strong chromophores. The iodine ir fluorescence quenching in liquid solvents thus represents a special case of the Förster energy transfer mechanism, which may prove important in other systems.

## V. CONCLUSIONS

We have presented the condensed phase spectroscopy and photodynamics of the doubly spin excited states of iodine. Although these states are strictly repulsive in the free molecule, in the solid state they are permanently bound by the cage potential and relax through radiation, while in the liquid phase they form transient contact pairs. The latter can be observed through the dipole allowed transitions that link  $I^*I^*$  to  $I^*I$ , a process absent in the separated atoms.

The solid state spectra allow the interrogation of cage potentials, and therefore the many-body I-Rg interactions, which, except for the  $I_2(B)$  state, are comparable to the iodine intramolecular interactions for the studied states. Given the open shell nature of the atoms involved, the description of these interactions is nontrivial. We have shown that the DIM approach for constructing these surfaces is quite useful, quantitatively correct in the case of Ar and at least qualitatively correct in the case of Kr and Xe. For this comparison, we have used the DIM potentials calculated by Batista and Coker for  $I_2$  isolated in the doubly substituted site of the perfect lattice.<sup>17</sup> A more rigorous test of the potential construct would require the consideration of lattice relaxation around the emitting state, which we have not carried out in the present.

As strictly transient pairs, the photodynamics of spin-excited atom pairs in the liquid phase is quite fascinating. Given the fact that once formed these pairs cannot recombine, they provide an opportunity for investigating caging dynamics without the interferences that arise in the case of ground state atoms which are connected asymptotically by a multiplicity of bound and unbound surfaces. In the present we have observed emission from both geminate and non-geminate contact pairs, the contact distance of which is controlled by the density of the solvent. Further, we have demonstrated that besides radiation, the contact pair undergo nonradiative decay through Förster transfer to the solvent. The CH vibrational overtones play the role of acceptors. Unlike the usual long-range nature of this process, due to the weak transition dipoles of both donor and acceptor, the transfer occurs between  $I^*I^*$  and first solvation shell.

Finally, the near ir emission from  $I^*I^*$  is a valuable tool for time resolved pump-probe investigations of dynamics in the lower manifold of the molecule. Such investigations have been implemented, both in liquids and solids, and will be reported in subsequent papers.

## ACKNOWLEDGMENTS

We gratefully acknowledge the support by AFOSR, under a University Research Initiative Grant No. F49620-1-0251, which made this work possible. We thank V. Batista and D. Coker for providing us the DIM potentials of  $I_2$  isolated in rare gas solids.

- <sup>1</sup>R. M. Bowman, M. Dantus, and A. H. Zewail, *Chem. Phys. Lett.* **161**, 297 (1989).
- <sup>2</sup>M. Gruebele, G. Roberts, M. Dantus, and A. H. Zewail, *Chem. Phys. Lett.* **166**, 459 (1990); M. Dantus, R. M. Bowman, and A. H. Zewail, *Nature (London)* **343**, 737 (1990).
- <sup>3</sup>R. Zadayan, Z. Li, P. Ashjian, C. C. Martens, and V. A. Apkarian, *Chem. Phys. Lett.* **218**, 504 (1994); Z. Li, R. Zadayan, V. A. Apkarian, and C. C. Martens, *J. Phys. Chem.* **99**, 7453 (1995).
- <sup>4</sup>R. Zadayan, Z. Li, C. C. Martens, and V. A. Apkarian, *J. Chem. Phys.* **101**, 6648 (1994); R. Zadayan, M. Sterling, and V. A. Apkarian, *J. Chem. Soc. Faraday Trans.* **92**, 1821 (1996).
- <sup>5</sup>A. L. Harris, M. Berg, and C. B. Harris, *J. Chem. Phys.* **84**, 788 (1986); M. E. Paige and C. B. Harris, *Chem. Phys.* **149**, 37 (1990).
- <sup>6</sup>See, for example, A. L. Harris, J. K. Brown, and C. B. Harris, *Annu. Rev. Phys. Chem.* **39**, 341 (1988).
- <sup>7</sup>Mulliken, *J. Chem. Phys.* **55**, 288 (1971). See also potentials constructed by Batista and Coker, Ref. 17.
- <sup>8</sup>R. Engelman, B. A. Palmer, and S. J. Davis, *J. Opt. Soc. Am.* **73**, 1585 (1983).
- <sup>9</sup>M. Macler, J.-P. Nicolai, and M. C. Heaven, *J. Chem. Phys.* **91**, 674 (1989).
- <sup>10</sup>R. Bohling, J. Langen, and U. Schurath, *Chem. Phys.* **130**, 419 (1989).
- <sup>11</sup>W. G. Lawrence and V. A. Apkarian, *J. Chem. Phys.* **101**, 1820 (1994).
- <sup>12</sup>M. Macler and M. C. Heaven, *Chem. Phys.* **151**, 219 (1991).
- <sup>13</sup>P. B. Beeken, E. A. Hanson, and G. W. Flynn, *J. Chem. Phys.* **78**, 5892 (1983).
- <sup>14</sup>A. L. Guy, K. S. Viswanathan, A. Sur, and J. Tellinguisen, *Chem. Phys. Lett.* **73**, 582 (1980).
- <sup>15</sup>J. C. D. Brand and A. R. Hoy, *Appl. Spectrosc. Rev.* **23**, 285 (1987).
- <sup>16</sup>G. Herzberg, *Spectra of Diatomic Molecules* (Van Nostrand Reinhold, New York, 1950).
- <sup>17</sup>V. S. Batista and D. F. Coker, *J. Chem. Phys.* **105**, 4033 (1996); *ibid.* (submitted).
- <sup>18</sup>The value of  $r_c$  does not bear any physical meaning, because this parameter depends on what functional form is used to represent the I-RG interaction. However, the equilibrium distance in the upper state  $r_e$ , determined by the spectral fit, is not sensitive to the specific functional form used in Eqs. (6) and (7).
- <sup>19</sup>L. Onsager, *J. Am. Chem. Soc.* **58**, 1486 (1936).
- <sup>20</sup>R. Fulton, *J. Chem. Phys.* **61**, 4141 (1974).
- <sup>21</sup>Th. Förster, *Ann. Phys.* **2**, 55 (1948); *Discuss. Faraday Soc.* **27**, 7 (1959).
- <sup>22</sup>L. Stryer, *Ann. Rev. Biochem.* **47**, 819 (1987).
- <sup>23</sup>M. A. Winnik, L. Li, and Y. S. Liu, in *Microchemistry*, edited by H. Masuhara (Elsevier, Amsterdam, 1994); A. Dhinojwala and J. M. Torkelson, *Macromolecules* **27**, 4817 (1994).
- <sup>24</sup>P. K. Wolber and B. S. Hudson, *Biophys. J.* **28**, 197 (1979); I. Yamazaki, N. Tamai, and T. Yamazaki, *J. Phys. Chem.* **94**, 516 (1990).
- <sup>25</sup>K. U. Finger, A. H. Marcus, and M. D. Fayer, *J. Chem. Phys.* **100**, 271 (1994); M. N. Berberan-Santos, M. J. E. Prieto, and A. G. Szabo, *J. Chem. Soc. Faraday Trans.* **88**, 255 (1992).